Bone 129 (2019) 115051

Contents lists available at ScienceDirect

Bone

journal homepage: www.elsevier.com/locate/bone

Full Length Article

Predicting experimentally-derived failure load at the distal radius using finite element modelling based on peripheral quantitative computed tomography cross-sections (pQCT-FE): A validation study

Hongyuan Jiang[a], Dale L. Robinson[b], Matthew McDonald[c], Peter V.S. Lee[b], Saija A. Kontulainen[e], James D. Johnston[c], Christopher J. Yates[a,d,f], John D. Wark[a,d,f,*]

[a] Department of Medicine, Royal Melbourne Hospital, University of Melbourne, Melbourne, Australia
[b] Department of Biomedical Engineering, University of Melbourne, Melbourne, Australia
[c] Department of Mechanical Engineering, University of Saskatchewan, Saskatoon, Canada
[d] Department of Diabetes and Endocrinology, Royal Melbourne Hospital, Melbourne, Australia
[e] College of Kinesiology, University of Saskatchewan, Saskatoon, Canada
[f] Bone and Mineral Medicine, Royal Melbourne Hospital, Melbourne, Australia

ARTICLE INFO

Keywords:
pQCT
Finite element modelling
Mechanical testing
Model validation
Cadaver

ABSTRACT

Dual energy X-ray absorptiometry, the current clinical criterion method for osteoporosis diagnosis, has limitations in identifying individuals with increased fracture risk, especially at the distal radius. Peripheral quantitative computed tomography (pQCT) can provide volumetric bone density data, as well as information on bone geometry, which makes it possible to establish finite element (FE) models of the distal radius from which bone strength and stiffness can be calculated. In this study, we compared experimental mechanical failure load data of the forearm with pQCT- based FE (pQCT-FE) modelling properties. Sixteen cadaveric forearm specimens were experimentally loaded until failure. Estimated stiffness and strength variables of compression, shear, bending and torsion were calculated from pQCT-FE modelling of single cross-sections of 0.2 × 0.2 × 2.4 mm of the radius pQCT image. A moderate-to-strong coefficient of determination (r^2) was observed between experimental failure load and pQCT-FE variables. The highest r^2 was observed for bending stiffness ($r^2 = 0.83$). This study validates the use of pQCT-FE in the assessment of distal radius bone strength for future studies.

1. Introduction

The prevalence of osteoporosis and subsequent fragility fractures (i.e. a fracture resulting from a minimal trauma such as a fall from a standing height or less. All fracture refers to fragility fracture in the following paragraphs) is increasing worldwide mainly due to population ageing [1,2]. A key to reducing this great public health burden is to identify individuals with increased risk for compromised bone strength (e.g., failure load, stiffness). The most established tool for the assessment of fracture risk is based on areal bone mineral density (aBMD) determined by dual energy x-ray absorptiometry (DXA), which is utilised in various algorithms for the calculation of absolute fracture risk [3–5]. However, DXA has limitations in the assessment of bone strength. On one hand, as a projective technique, it does not take bone volume adequately into consideration; rather it provides an 'areal' bone mineral density (aBMD) in g/cm^2, which represents the bone mineral content within a projected area of bone. On the other hand, bone failure strength is determined not only by bone quantity, but also by how trabecular bone is spatially distributed [11], which is not represented well by conventional DXA measures. Previous studies have observed that DXA measurements only explain part of bone strength, with r^2 ranging from 0.31 to 0.56 between different DXA variables and failure load of the radius in falling configurations [7–10]. Therefore, alternate clinically-relevant fracture risk assessment strategies are needed at the distal radius.

Other than bone quantity, bone quality also contributes strongly to bone strength [11]. As one aspect of bone quality, bone geometry e.g. bone size, cortical thickness, bone cross-sectional area etc. are closely associated with bone failure load and fracture occurrence [6,12]. Therefore, bone density and bone geometry together should contribute to the understanding of bone strength. Peripheral quantitative computed tomography (pQCT), a CT scanner that is specifically used to

* Corresponding author at: Department of Medicine, Royal Melbourne Hospital, University of Melbourne, Parkville, Victoria 3052, Australia.
E-mail address: jdwark@unimelb.edu.au (J.D. Wark).

https://doi.org/10.1016/j.bone.2019.115051
Received 12 June 2019; Received in revised form 6 August 2019; Accepted 27 August 2019
Available online 28 August 2019

image the radius and tibia, is able to measure bone geometry, e.g. bone cross-sectional area, second moment of inertia (I), cortical thickness, as well as volumetric bone mineral density (vBMD). All these pQCT properties should contribute to our understanding of bone fragility. Indeed, more patients with low-trauma fracture can be identified as high-risk for osteoporosis using conventional pQCT measures combined with DXA T-scores when compared with DXA measures alone [13]. More recently, we established the potential of finite element analysis based on tibial pQCT images for the classification of fracture status in a clinical setting [14]. As a large proportion of low-trauma fractures occur at the distal radius, pQCT was anticipated to be an ideal tool for the assessment of bone strength at this clinically-important site.

Due to the volumetric bone measurements acquired by pQCT, it is an ideal imaging modality to be utilised with FE modelling. Previously, FE models of sites of clinical interest e.g. vertebrae and femur, have been developed based on quantitative computed tomography (QCT) using a clinical CT scanner and bone density phantom [15,16], or magnetic resonance imaging (MRI) scanner [17]. During the past decade, FE models based on high-resolution pQCT (HR-pQCT) have also emerged in the assessment of the tibia or radius strength [10,18,19]. While providing good prediction for bone strength, these modalities do have some drawbacks. QCT has relatively high radiation exposure to scan the whole spine or limb [20]. While HR-pQCT has comparable radiation exposure with pQCT, it is time-consuming to scan and set up individual FE models from HR-pQCT images [21], as well as QCT images. While MRI does not expose the patients to radiation, its cost and prolonged imaging sequences limit its clinical use and applications in large populations and, more importantly, the extremely short lifetime of the MR signal for water bound to hard tissue, makes the quantification of cortical mineralization difficult [22].

Similarly, issues of long scanning time, relatively high radiation exposure and extended individual model set-up times exist for pQCT to scan the whole forearm, which makes it impractical in clinical settings. FE models based on single pQCT cross-sections may solve the aforementioned issues. pQCT is designed for measurement of the site where a distal radius fracture occurs (e.g., Colles' fracture) [23]. This scanning location, together with its sufficient resolution for FE modelling and reasonable scanning time for one cross-section with low radiation exposure, makes pQCT a potentially-attractive choice as a data source for individually set-up FE models. While not based on the whole radius properties, strength and stiffness predicted at a discrete location of a single pQCT cross-section may be proportional to the strength of the entire forearm, which may be utilised for more effective, yet rapid assessment of fracture risk.

In this study, we present a pQCT-derived FE analysis technique (pQCT-FE) to estimate bone strength and stiffness of individual cross-sections of the distal radius obtained from clinical pQCT images. For validation purposes, these strength and stiffness estimates were correlated against experimental testing of the forearm in loading configurations mimicking a Colles' fracture. We focus on distal radius fracture only here due to the fact that distal radius is a clinically-important site where a large proportion of fragility fractures were estimated to occur [24,25]. More importantly, fragility fracture is also an early sign of compromised bone strength and is associated with occurrence of further fracture [26,27]. Therefore, improvement in understanding bone fragility at this site may help identifying more patients with osteoporosis at an earlier stage. We hypothesized that pQCT-FE properties could explain a large proportion of variance in the overall bone failure load, thus demonstrating the potential utility of this method for the assessment of bone fracture risk in vivo.

2. Methods

Information regarding specimen acquisition, preparation and mechanical testing is outlined in detail elsewhere [28,29]. Details are briefly summarized below.

2.1. Specimens

Twenty-one fresh human cadaver forearms (7 left, 14 right) from 21 female donors were obtained from an anatomical tissue bank. Specimens with no history of fracture or bone disease were selected. Donors' age at death was 81.7 ± 9.3 years, height was 161.4 ± 5.3 cm, weight was 58.9 ± 9.2 kg and body mass index (BMI) was 22.6 ± 3.2 kg/m^2. All specimens were kept intact, were fresh frozen at −20 °C, and thawed for imaging and mechanical testing. This study was approved by the University of Saskatchewan Biomedical Research Ethics Board.

2.2. Peripheral quantitative computed tomography scanning

A single 2.4 mm slice was acquired at the 4% site of the radius length, measured proximally to the distal articular surface, using an XCT 2000 pQCT scanner (Stratec Medizintechnik GmbH, Pforzheim, Germany) and our clinical scanning protocol [30]. Radius length was measured from the proximal and lateral border of the head of the radius to the most distal point of the lateral margin of the styloid process of the radius. A scout view over the distal joint was performed from which a reference line at the medial tip of the distal endplate of the radius was set as the starting plane. An in-plane pixel size of 0.2 mm by 0.2 mm was obtained. Scanning speed was 10 mm/s. A commercial BMD phantom made by the scanner manufacturer was employed daily prior to scanning to maintain quality assurance.

2.3. Mechanical testing

After pQCT imaging, cadaveric forearms were prepared for mechanical testing. Soft tissue was removed from around the radius and ulna, then their midshafts were potted in polymethylmethacrylate (PMMA) according to the method proposed by Edwards and Troy [31]. The potted forearm was clamped to the base of a servo-hydraulic material testing machine (MTS Bionix Servohydraulic Testing System), which compressed a flat plate attached to the piston against the outstretched palm of each specimen [28,29]. For the loading configuration, 21 specimens were positioned off-axially with 15° dorsal inclination [32] and 3–6° radial inclination. The palm was set flat against the testing plate and perpendicular to the vertical loading axis.

Compression was conducted in displacement control to failure at a rate of 3 mm/s. Failure loads (F_{exp}, N) were calculated from the load-displacement curve, where failure load was defined as the maximum load on the load-displacement curve. The linear region for the stiffness calculation was identified by visual inspection and confirmed by manually fitting a linear regression curve ($r^2 > 0.99$) to the load-displacement curve.

2.4. Finite element analysis

All pQCT images were exported to Matlab software (2017a, Mathworks, Natick, MA, USA) for manual segmentation. A mesh of 0.2 × 0.2 × 2.4 mm elements was generated from segmentation, and then reconstructed in the axial plane to produce 0.2 × 0.2 × 0.2 mm elements. Each element (numbered i) was modeled as a linear elastic material with a Poisson's ratio of 0.3 and the respective apparent bone mineral density ($\rho_{app,i}$) and Young's modulus (E_i) calculated using Eqs. (1) and (2) [31,33].

$$\rho_{app,i} = 1.484 H_{f,i} - 48965 \quad (1)$$

$$E_i = 2875 \rho_{app,i}{}^3 \quad (2)$$

where $\rho_{app,\,i}$, E_i and $H_{f,i}$ are the apparent bone mineral density (g/cm^3), Young's modulus (MPa) and the Hounsfield unit of each individual voxel i (HU), respectively.

Each voxel mesh was used to generate a FE model in Abaqus (V6.11,

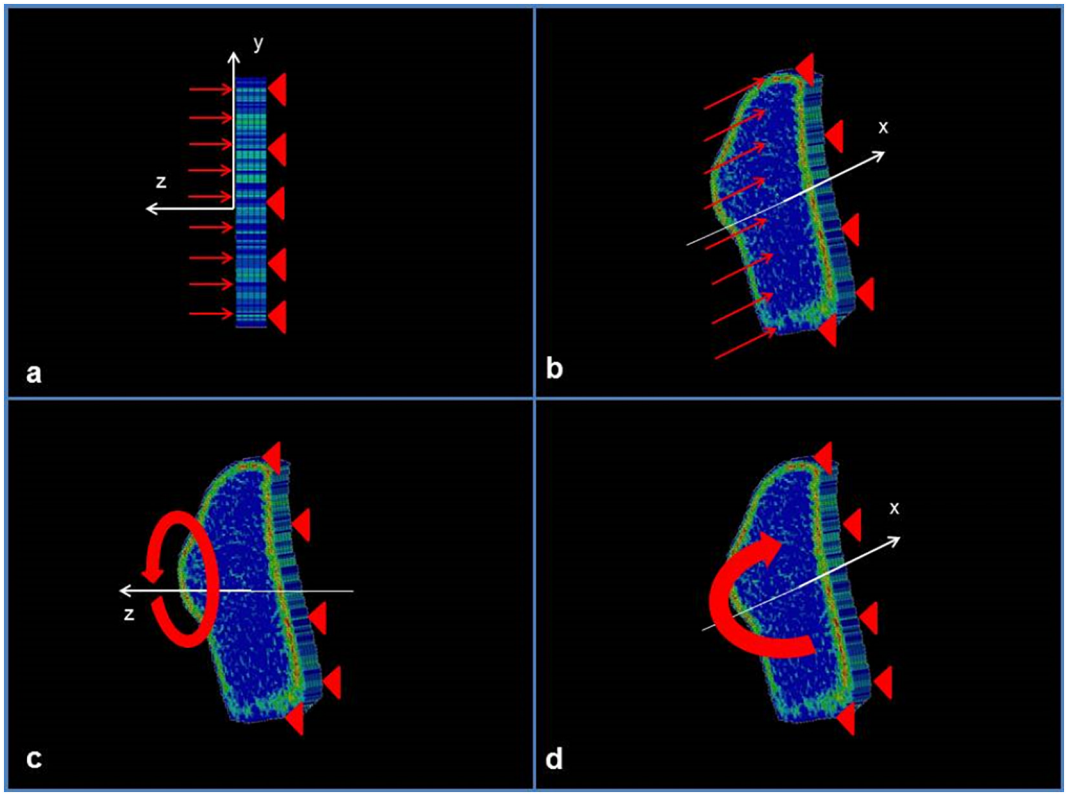

Fig. 1. Four loading cases simulated in pQCT-FE model. Axial compression (a) was simulated by a 0.01 mm displacement of the superior surface towards the inferior surface. Shear (b) was simulated by a 0.01 mm displacement of the superior surface in the direction of either the x- or y-axes. Torsion (c) was simulated by a 0.0001 radian rotation of the inferior surface about the z-axis. Bending (d) was simulated by a 0.0001 radian rotation of the inferior surface about either the x- or y-axes (i.e., cross-section neutral axes).

2011, Simulia, Dassault Systemes, Providence, RI, USA), with each element represented by a fully-integrated 8 node hexahedron. The origin of the models was set as the density-weighted centroid (Eqs. (3) and (4)), where the x- and y-axes were aligned with the minimum and maximum neutral axes, respectively, and the z-axis was normal to the cross-section.

$$\bar{x} = \frac{\sum E_i x_i a_i}{\sum a_i} \tag{3}$$

$$\bar{y} = \frac{\sum E_i y_i a_i}{\sum a_i} \tag{4}$$

where a_i is the area of voxel i. $\bar{x}$, $\bar{y}$ are the coordinates of the density-weighted centroid for the cross-section, and x_i, y_i represent the horizontal and vertical distance between voxel i and the density-weighted centroid.

Four loading cases were considered for all FE Models: axial compression, shear, bending, and torsion (Fig. 1), each considered as a quasi-static simulation with the assumption of small deformation. Axial compression was simulated by a 0.01 mm displacement of the superior surface towards the inferior surface. Shear was simulated by a 0.01 mm displacement of the superior surface in the direction of either the x- or y-axes. Bending was simulated by a 0.0001 radian rotation of the inferior surface about either the x- or y-axes (i.e., cross-section neutral axes). Torsion was simulated by a 0.0001 radian rotation of the inferior surface about the z-axis.

Stiffness and strength were calculated for each loading case for each specimen. The reaction forces and moments predicted from the simulations were divided by the respective applied displacement or rotation to derive the compressive stiffness (k_{comp}), shear stiffness (k_{shear}), bending stiffness (k_{bend}), and torsional stiffness ($k_{torsion}$) of each cross-section. The bending and shear stiffness were each taken as the minimum value derived from the two neutral-axis directions. The minimum compressive and maximum tensile principal strains predicted for each simulation (ε_{max} and ε_{min}, respectively) were compared with compressive and tensile yield strains reported for the radius (1.10% and 0.66%, for compression and tension, respectively [31]) to derive a factor-of-safety. The factor-of-safety was multiplied by the respective reaction force or moment to derive the strength for compression (S_{comp}), shear (S_{shear}), bending (S_{bend}) and torsion ($S_{torsion}$), of each cross-section.

2.5. Statistical analysis

Descriptive data were expressed as mean ± 1.0 standard deviation (SD). A linear regression model was developed to correlate each pQCT-FE stiffness and strength variable with failure load (F_{exp}) measured from the mechanical testing, from which the coefficient of determination (r^2) was calculated. Additional regression models were also developed for each pQCT-FE variable after adjustment for age, i.e. set age and each pQCT stiffness/strength variable as independent factors while failure load as the dependent factor in the regression models. Level of significance for all analyses was set as $p < 0.05$. All statistical analyses were performed using SPSS 22.0 (SPSS Inc., Chicago, IL, USA).

3. Results

After loading, 5 specimens did not experience a distal radius fracture and were excluded from further analysis. Alternate failure mechanisms included a scaphoid fracture (n = 1) and midshaft fractures originating at the potting (n = 4). They were excluded from analysis as pQCT scans were not obtained at these locations. Therefore, it would be incompatible for the FE model to attempt to predict the bone strength at these locations. Furthermore, these fractures do not represent a

Table 1
Means and SDs of pQCT-FEA variables and corresponding coefficients of determination (r^2) against failure load before and after adjustment for age. All correlations had a significance of $p < 0.01$.

FEA variable	Mean ± SD	r^2	r_{adj}^2
k_{comp} (kN/mm)	198.0 ± 60.7	0.66	0.77
k_{shear} (kN/mm)	46.3 ± 16.2	0.64	0.77
k_{bend} (Nm/deg)	85.7 ± 31.3	0.83	0.86
$k_{torsion}$ (Nm/deg)	69.4 ± 27.3	0.81	0.85
S_{comp} (N)	3.5 ± 1.3	0.56	0.69
S_{shear} (10^2 N)	3.1 ± 1.1	0.46	0.67
S_{bend} (Nm)	4.1 ± 1.5	0.71	0.79
$S_{torsion}$ (Nm)	2.5 ± 1.0	0.64	0.77

k_{comp}, compression stiffness; k_{shear}, shear stiffness; k_{bend}, bending stiffness; $k_{torsion}$, torsion stiffness, S_{comp}, compression strength; S_{shear}, shear strength, S_{bend}, bending strength; $S_{torsion}$, torsion strength, r^2, coefficient of determination before adjustment for age; r_{adj}^2, coefficient of determination after adjustment for age.

common type of fragility fracture, and were beyond the topic of this study.

Alternate failure mechanisms brought the sample to 16 specimens [28,29]. The mean ± SD age of this analysis sample was 81.6 ± 9.9 years. In terms of fracture types, the majority were Colles' type (n = 14) combined with compressive-type fractures (n = 2). A Colles' type fracture was defined as a transverse fracture ~25–40 mm proximal to the radio-carpal joint, with evidence of dorsal displacement and angulation of the distal fragment, radial shortening, and loss of radial inclination and palmar tilt [34,35]. A compressive-type fracture was defined as a transverse fracture ~25–40 mm proximal to the radio-carpal joint with evidence of radial shortening. Fracture classification was based upon visual assessment by a single researcher (MM). In terms of limb distribution, there were 5 left and 11 right limbs included in the analysis.

The pQCT-FE stiffness and strength properties of the cadaveric radii and the corresponding r^2 when regressed against the experimental failure load are summarized in Table 1, and visual representation of each regression is shown in Fig. 2. Medium-to-strong r^2 values were observed for experimental failure load regressed against each of the FE-derived stiffness variables, which were $r^2 = 0.66$, 0.64, 0.83 and 0.82 for k_{comp}, k_{shear}, k_{bend} and $k_{torsion}$, respectively (all $p < 0.01$). Similar trends for r^2 were found for experimental failure load regressed against FE-derived strength variables, where $r^2 = 0.56$, 0.46, 0.71 and 0.64 for S_{comp}, S_{shear}, S_{bend} and $S_{torsion}$, respectively (all $p < 0.01$). All r^2 tended to improve after regression models were adjusted for age, with highest $r^2 = 0.86$ and 0.79 for k_{bend} and S_{bend}, respectively.

4. Discussion

Due to the great economic and societal burden of osteoporosis and the consequent fractures, and the limitations of DXA in identifying individuals with increased fracture risk, it is necessary to find a complementary tool providing information about bone strength additional to DXA. In this study, we sought to validate a pQCT-FE model that could be used to supplement assessment of bone strength using DXA alone. Medium to strong r^2 values were observed between experimental failure load and pQCT-FE properties, ranging from 0.64 to 0.83 for pQCT-FE stiffness variables, and 0.46 to 0.71 for pQCT-FE strength variables. Improvement in r^2 was also observed after the regression models were adjusted for age, with r_{adj}^2 ranging from 0.77 to 0.86 for pQCT-FE stiffness variables, and 0.64 to 0.79 for pQCT-FE strength variables. These r^2 were found to be higher than those between DXA radius variables and forearm fracture failure in mechanical testing with similar falling configurations, which were 0.31–0.56 from the literature [7–10].

Among the pQCT-FE properties of the four load cases, bending properties had the highest contribution to variance in experimental failure load for both stiffness and strength variables, with $r_{adj}^2 = 0.86$ and 0.79, respectively. This was likely to be due to the imposed loading configuration, where the radius long axis was offset 15° from the loading axis, thus imparting a combination of compression and bending on the radius. It may also explain why the pQCT-FE shearing properties accounted for the least variance in failure load among the four load cases since the off-axis compression is unlikely to generate a high shear load. This is pertinent to the real-world situation as Colles' fractures are believed to be the result of bending, rather than other types of loading vectors i.e. compression, torsion or shearing [36–38].

Areal BMD measured by DXA accounts for only part of the variance in bone failure load. The r^2 between bone failure load and aBMD differed in various studies but generally ranged between 0.34 and 0.64 at standard imaging sites [39–42]. When it comes to the radius, DXA is reported to account for no more than 60% of variation in forearm strength. Higher r^2 was reported in the current study between radius mechanical failure load and pQCT-FEA stiffness, with highest r^2 of 0.86. These results suggest that our pQCT FE models provide improved bone strength assessment compared to previous estimates based on DXA.

More recently, micro FE (μFE) models based on HR-pQCT with voxel size of 85 μm, which enables depiction of the trabecular microstructure of the radius and tibia, emerged in clinical research [18]. Outputs from these models have demonstrated an improved ability to classify fracture status of patients compared to DXA [43], and good correlations have been observed when predicting experimental failure loads of cadaveric radii, with r^2 of 0.70–0.92 [10,44,45]. Although these previous r^2 findings describe a different testing configuration to the off-axis loading in the current study, they provide insight into our understanding of bone fragility explained by different tools. In a study comparing HR-pQCT μFE and QCT FE which is based on volumetric data of similar resolution to pQCT in the prediction of femur failure load, HR-pQCT μFE predicted failure load similarly to QCT FE ($r^2 = 0.86$ vs $r^2 = 0.84$, respectively) [46]. HR-pQCT has other drawbacks, such as exposing patients to slightly higher radiation than pQCT, and due to its higher resolution, it is time-consuming to process the large volume of imaging data in the FE analysis [21]. More importantly, HR-pQCT, as a newer technique than pQCT, is not widely available due to its prohibitive cost.

This study has several limitations. Peripheral QCT images with a voxel size of 0.2 mm and slice thickness of 2.4 were obtained to generate a cross-sectional FE model for each specimen. Compared to the voxel size of HR-pQCT (85 μm) which can depict the micro-structure of the radius, the voxel size of pQCT (200 μm) is relatively large and is not precise enough to reflect the topology of individual trabeculae. However, this resolution appears to be sufficient to allow prediction of the variance in experimental failure load of the radius according to previous studies [47–49]. In these studies, 0.25–1.08 mm voxels from QCT images were used to establish FE models of the femur, and simplified trabeculae topology as a continuum FE mesh as in the current study was used with similar element sizes. Strong coefficients of determination were observed between these QCT FE variables and mechanical failure load in the laboratory, ranging from 0.74 to 0.90. Strong r^2 between pQCT-FEA variables and radius failure load in the current study support the argument that resolution of 0.2 mm voxels can explain a high proportion of the variance in the whole bone properties.

FE strength and stiffness were calculated from four loading cases in this study; however, a loading combination of compression, torsion, bending and shear occurs at the same time in vivo [50]. The individual loading cases may be too idealised for the assessment of bone strength, but similar to the barrel analogy of Liebig's law of the minimum, where the shortest stave decides the capacity of a barrel with staves of unequal lengths, a bone's strength is limited by the weakest resistance of an idealised loading condition. This logic was reflected in previous studies, where the radius strength for fracture risk assessment was measured by

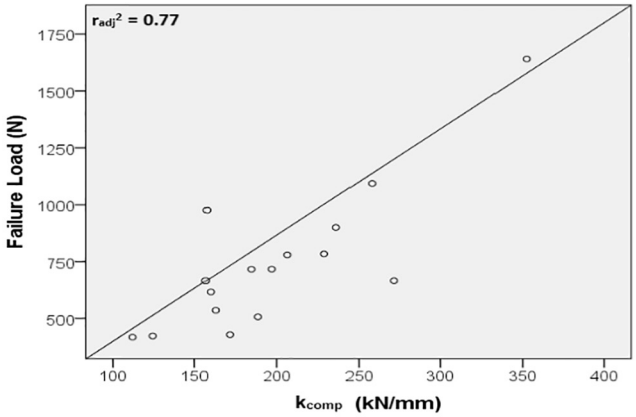

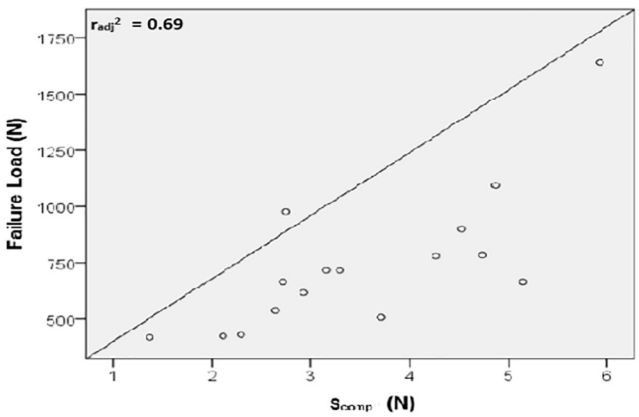

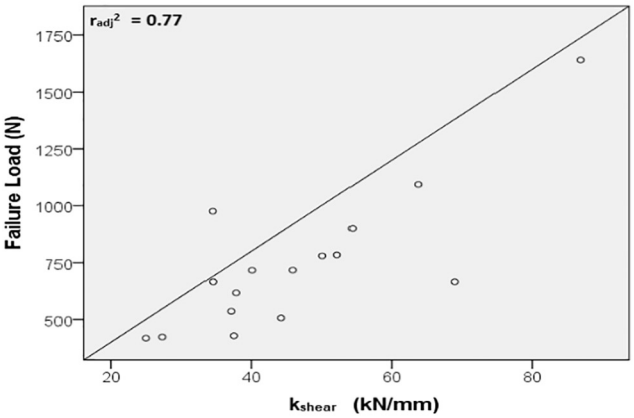

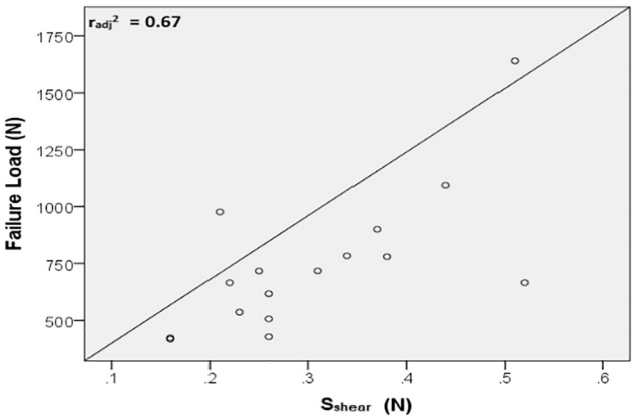

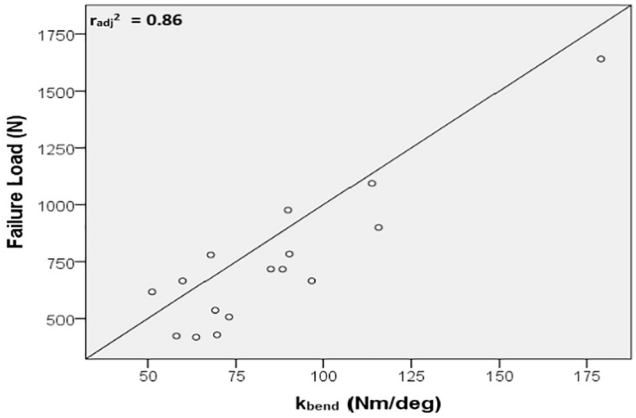

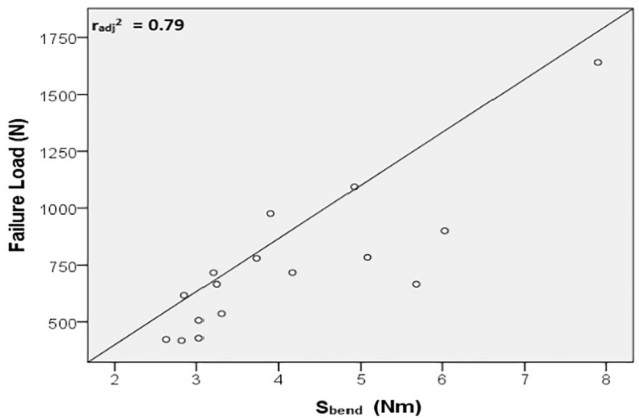

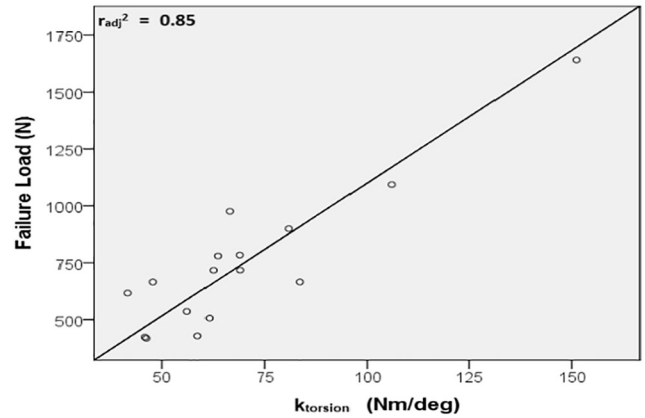

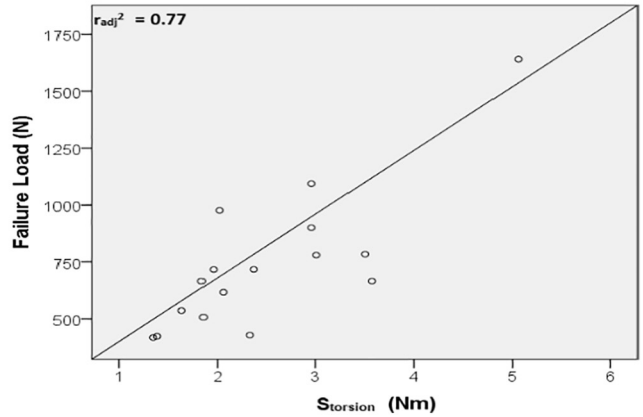

(caption on next page)

Fig. 2. Scatter plots of pQCT-FE properties against experimental failure load. r^2: coefficient of determination before adjustment for age, r_{adj}^2: coefficient of determination after adjustment for age.
k_{comp}: compression stiffness; S_{comp}: compression strength; k_{shear}: shear stiffness; S_{shear}: shear strength; k_{bend}: bending stiffness; S_{bend}: bending strength; $k_{torsion}$: torsion stiffness; $S_{torsion}$: torsion strength.

idealised axial compression only [51]. Indeed, we did not intend to calculate the real radius strength or stiffness from the pQCT-FE, rather we presented an idealised loading scenario that could be easily constructed, and it was assumed that strength and stiffness from one cross-section would be proportional to the whole bone failure under more complex loading configurations.

As discussed previously, bone quality contributes to bone strength [11,52]. Properties of bone quality other than bone geometry, e.g. degree of bone mineralization, hydroxyapatite crystal size and heterogeneity, collagen properties and osteocyte density are considered determinants of bone strength; however unfortunately, these bone properties are not available using standard pQCT imaging and require detailed analysis of bone biopsies. The feasibility of using bone biopsies to identify fracture risk is challenging as it is invasive and likely difficult to recruit otherwise healthy patients to undergo this procedure. The advantage of the current method is that it is readily available as it can be applied to existing clinical pQCT imaging methods.

Following the exclusion of 5 specimens for undesirable material behaviors during testing, there was a reduced number of specimens (n = 16), which would have lessened the statistical power of our analysis. However, the final sample size was sufficient for strong univariate correlations to be found in the models where r^2 was calculated. In addition, the mean age of donors in this study (82 ± 10 years) was greater than the average ages reported for forearm fracture (71 ± 15 years [53,54]). However, after adjustment for age, improvement was observed in all correlations between experimental and pQCT-FE properties. This provides better prospect for the pQCT-FE models although sample size was limited. Further studies with a larger sample size may help improve the multivariate regression models.

In summary, we experimentally validated a pQCT image-based FE method for the assessment of bone strength at the clinically-relevant distal radius site. As much as 86% of variance in experimental radius failure load was explained by pQCT-FE properties. This FE model makes individual assessment of bone strength at a site with a propensity for osteoporotic fracture more accessible by using a widely-available device with reasonable scanning time and low radiation. Future research may focus on this technique's role in differentiating patients with increased fracture risk from the healthy in clinical settings.

Acknowledgements

We thank all study donors who bequeathed their bodies for medical science. We wish to acknowledge Dr. Chantal Kawalilak, Nima Ashjaee and Amy Bunyamin for assistance with mechanical testing and specimen preparation.

Declaration of competing interest

None.

Funding

This work was supported by the Natural Sciences and Engineering Research Council of Canada (NSERC Discovery Grant RGPIN-2016-05301, SK) and Saskatchewan Health Research Foundation (SHRF Establishment Grant 2632, JDJ). HJ was funded under a joint PhD scholarship by China Scholarship Council (funding reference: CSC201608240003) and the University of Melbourne.

Ethical approval

This study involves use of human cadaver and was approved by the University of Saskatchewan Biomedical Research Ethics Board (Ethics number 09-96).

References

[1] J.A. Kanis, E.V. McCloskey, H. Johansson, C. Cooper, R. Rizzoli, J.Y. Reginster, Scientific Advisory Board of the European Society for Clinical and Economic Aspects of Osteoporosis and Osteoarthritis (ESCEO) and the Committee of Scientific Advisors of the International Osteoporosis Foundation (IOF). European guidance for the diagnosis and management of osteoporosis in postmenopausal women, Osteoporos. Int. 24 (1) (2013) 23–57.
[2] L.F. Baccaro, D.M. Conde, L. Costa-Paiva, A.M. Pinto-Neto, The epidemiology and management of postmenopausal osteoporosis: a viewpoint from Brazil, Clin. Interv. Aging 10 (2015) 583–591.
[3] N.D. Nguyen, S.A. Frost, J.R. Center, J.A. Eisman, T.V. Nguyen, Development of prognostic nomograms for individualizing 5-year and 10-year fracture risk, Osteoporos. Int. 19 (10) (2008) 1431–1444.
[4] J.A. Kanis, A. Oden, H. Johansson, F. Borgstrom, O. Strom, E. McCloskey, FRAX and its applications to clinical practice, Bone 44 (5) (2009) 734–743.
[5] B. Ettinger, H. Liu, T. Blackwell, A.R. Hoffman, K.E. Ensrud, E.S. Orwoll, Osteoporotic Fracture in Men (MrOS) Research Group. Validation of FRC, a fracture risk assessment tool, in a cohort of older men: the Osteoporotic Fractures in Men (MrOS) Study, J. Clin. Densitom. 15 (3) (2012) 334–342.
[6] H. Fonseca, D. Moreira-Goncalves, M. Vaz, et al., Changes in proximal femur bone properties following ovariectomy and their association with resistance to fracture, J. Bone Miner. Metab. 30 (3) (2012) 281–292.
[7] P. Augat, H. Iida, Y. Jiang, E. Diao, H.K. Genank, Distal radius fractures: mechanism of injury and strength prediction by bone mineral assessment, J. Orthop. Res. 16 (1998) 629–635.
[8] C. Wu, D. Hans, Y. He, B. Fan, C.F. Njeh, P. Augat, J. Richards, H.K. Genant, Prediction of bone strength of distal forearm using radius bone mineral density and phalangeal speed of sound, Bone 26 (2000) 529–533.
[9] E.M. Lochmuller, C.A. Lill, V. Kuhn, E. Schneider, F. Eckstein, Radius bone strength in bending, compression, and falling and its correlation with clinical densitometry at multiple sites, J. Bone Miner. Res. 17 (9) (2002) 1629–1638.
[10] W. Pistoia, B. van Rietbergen, E.M. Lochmüller, C.A. Lill, F. Eckstein, P. Rüegsegger, Estimation of distal radius failure load with micro-finite element analysis models based on three-dimensional peripheral quantitative computed tomography images, Bone 30 (6) (2002) 842–848.
[11] H. Fonseca, Bone quality: the determinants of bone strength and fragility, Sports Med. 44 (1) (2014) 37–53.
[12] J.D. Alele, D.L. Kamen, K.J. Hunt, et al., Bone geometry profiles in women with and without SLE, J. Bone Miner. Res. 26 (11) (2011) 2719–2726.
[13] H. Jiang, C.J. Yates, A. Gorelik, A. Kale, Q. Song, J.D. Wark, Peripheral quantitative computed tomography (pQCT) measures contribute to the understanding of bone fragility in older patients with low-trauma fracture, J. Clin. Densitom. 21 (1) (2018) 140–147.
[14] D.L. Robinson, H. Jiang, Q. Song, C. Yates, P.V.S. Lee, J.D. Wark, The application of finite element modelling based on clinical pQCT for classification of fracture status, Biomech. Model. Mechanobiol. 18 (1) (2019) 245–260.
[15] G.U. Unnikrishnan, G.D. Barest, D.B. Berry, A.I. Hussein, E.F. Morgan, Effect of specimen-specific anisotropic material properties in quantitative computed tomography-based finite element analysis of the vertebra, J. Biomech. Eng. 135 (10) (2013) 101007–101011.
[16] A.L. Evans, M.A. Paggiosi, R. Eastell, J.S. Walsh, Bone density, microstructure and strength in obese and normal weight men and women in younger and older adulthood, J. Bone Miner. Res. 30 (5) (2015) 920–928.
[17] N. Zhang, J.F. Magland, C.S. Rajapakse, Y.A. Bhagat, F.W. Wehrli, Potential of in vivo MRI-based nonlinear finite-element analysis for the assessment of trabecular bone post-yield properties, Med. Phys. 40 (5) (2013) 52303.
[18] B. Van Rietbergen, K. Ito, A survey of micro-finite element analysis for clinical assessment of bone strength: the first decade, J. Biomech. 48 (5) (2015) 832–841.
[19] J.A. MacNeil, S.K. Boyd, Improved reproducibility of high-resolution peripheral quantitative computed tomography for measurement of bone quality, Med. Eng. Phys. 30 (6) (2008) 792–799.
[20] K. Engelke, J.E. Adams, G. Armbrecht, P. Augat, C.E. Bogado, M.L. Bouxsein, D. Felsenberg, M. Ito, S. Prevrhal, D.B. Hans, E.M. Lewiecki, Clinical use of quantitative computed tomography and peripheral quantitative computed tomography in the management of osteoporosis in adults: the 2007 ISCD official positions, J. Clin. Densitom. 11 (1) (2008) 123–162.
[21] C.E. Kawalilak, S.A. Kontulainen, M.A. Amini, J.L. Lanovaz, W.P. Olszynski, J.D. Johnston, In vivo precision of three HR-pQCT-derived finite element models of the distal radius and tibia in postmenopausal women, BMC Musculoskelet. Disord.

17 (1) (2016) 1–11.
[22] F.W. Wehrli, Magnetic resonance of calcified tissues, J. Magn. Reson. 229 (2013) 35–48.
[23] W.D. Leslie, S.N. Morin, Osteoporosis epidemiology 2013: implications for diagnosis, risk assessment, and treatment, Curr. Opin. Rheumatol. 26 (4) (2014) 440–446.
[24] O. Johnell, J.A. Kanis, An estimate of the worldwide prevalence and disability associated with osteoporotic fractures, Osteoporos. Int. 17 (2006) 1726.
[25] V.J. Sabesan, T. Valikodath, A. Childs, V.K. Sharma, Economic and social impact of upper extremity fragility fractures in elderly patients, Aging Clin. Exp. Res. 27 (4) (2015) 539–546.
[26] H. Mallmin, S. Ljunghall, I. Persson, T. Naessen, U.B. Krusemo, R. Bergstrom, Fracture of the distal forearm as a forecaster of subsequent hip fracture: a population-based cohort study with 24 years follow-up, Calcif. Tissue Int. 52 (1993) 269–272.
[27] C.M. Klotzenbeucher, P.D. Ross, P.B. Landsman, T.A. Abbott III, M. Berger, Patients with prior fractures have an increased risk of future fractures: a summary of the literature and statistical synthesis, J. Bone Miner. Res. 15 (2000) 721–739.
[28] J.D. Johnston, M. McDonald, S.A. Kontulainen, Off-axis loads cause failure of the distal radius at lower magnitudes than axial loads: an ex vivo experimental comparison between left and right forearms, (2019) (Manuscript submitted for publication).
[29] A. Hosseinitabatabaei, C.E. Kawalilak, M.P. McDonald, S.A. Kontulainen, J.D. Johnston, HR-pQCT based finite element modeling of distal radius failure load: relationship with ex vivo fall-configuration failure load and in vivo precision error, (2019) (Manuscript submitted for publication).
[30] R.L. Duckham, A.W. Frank, J.D. Johnston, W.P. Olszynski, S.A. Kontulainen, Monitoring time interval for pQCT-derived bone outcomes in postmenopausal women, Osteoporos. Int. 24 (2013) 1917–1922.
[31] W.B. Edwards, K.L. Troy, Finite element prediction of surface strain and fracture strength at the distal radius, Med. Eng. Phys. 34 (3) (2012) 290–298.
[32] E.R. Myers, E.A. Sebeny, A.T. Hecker, T.A. Corcoran, J.A. Hipp, S.L. Greenspan, W.C. Hayes, Correlations between photon absorption properties and failure load of the distal radius in vitro, Calcif. Tissue Int. 49 (1991) 292–297.
[33] M. Doube, M. Kłosowski, I. Arganda-Carreras, F.P. Cordelières, R.P. Dougherty, J.S. Jackson, B. Schmid, J.R. Hutchinson, S.J. Shefelbine, BoneJ: free and extensible bone image analysis in ImageJ, Bone 47 (6) (2010) 1076–1079.
[34] A. Colles, On the fracture of the carpal extremity of the radius, Edinb. Med. Surg. J. 10 (38) (1814) 182–186.
[35] C.A. Goldfarb, Y. Yin, L.A. Gilula, A.J. Fisher, M.I. Boyer, Wrist fractures: what the clinician wants to know, Radiology 219 (1) (2001) 11–28.
[36] A.H. Crenshaw, Fractures of shoulder girdle, arm, and forearm, in: S.T. Canale (Ed.), Campbell's Operative Orthopaedics, Mosby, St Louis, 1998, pp. 2281–2362.
[37] D.L. Fernandez, Distal radius fracture: the rationale of a classification, Chirurgie De La Main 20 (2001) 411–425.
[38] J.B. Jupiter, D.L. Fernandez, Comparative classification for fractures of distal end of the radius, J. Hand Surg. 22 (1997) 563–571.
[39] X.G. Cheng, P.H. Nicholson, S. Boonen, G. Lowet, P. Brys, J. Aerssens, G. Van der Perre, J. Dequeker, Prediction of vertebral strength in vitro by spinal bone densitometry and calcaneal ultrasound, J. Bone Miner. Res. 12 (10) (1997) 1721–1728.
[40] F. Eckstein, E.M. Lochmüller, C.A. Lill, V. Kuhn, E. Schneider, G. Delling, R. Müller, Bone strength at clinically relevant sites displays substantial heterogeneity and is best predicted from site-specific bone densitometry, J. Bone Miner. Res. 17 (1) (2009) 162–171.
[41] E. Perilli, A.M. Briggs, S. Kanor, J. Codrington, J.D. Wark, I.H. Parkinson, N.L. Fazzalari, Failure strength of human vertebrae: prediction using bone mineral density measured by DXA and bone volume by micro-CT, Bone 50 (6) (2012) 1416–1425.
[42] J. Mi, K. Li, X. Zhao, C.Q. Zhao, H. Li, J. Zhao, Vertebral body compressive strength evaluated by dual-energy x-ray absorptiometry and Hounsfield units in vitro, J. Clin. Densitom. 21 (1) (2018) 148–153.
[43] X.S. Liu, E.M. Stein, B. Zhou, C.A. Zhang, T.L. Nickolas, A. Cohen, V. Thomas, D.J. McMahon, F. Cosman, J. Nieves, E. Shane, X.E. Guo, Individual trabecula segmentation (ITS)-based morphological analyses and microfinite element analysis of HR-pQCT images discriminate postmenopausal fragility fractures independent of DXA measurements, J. Bone Miner. Res. 27 (2) (2012) 263–272.
[44] P. Varga, D.H. Pahr, S. Baumbach, P.K. Zysset, HR-pQCT based FE analysis of the most distal radius section provides an improved prediction of Colles' fracture load in vitro, Bone 47 (5) (2010) 982–988.
[45] T.L. Mueller, D. Christen, S. Sandercott, S.K. Boyd, B. van Rietbergen, F. Echstein, E.M. Lochmüller, R. Müller, G.H. van Lenthe, Computational finite element bone mechanics accurately predicts mechanical competence in the human radius of an elderly population, Bone 48 (6) (2011) 1232–1238.
[46] B. Luisier, E. Dall'Ara, D.H. Pahr, Orthotropic HR-pQCT-based FE models improve strength predictions for stance but not for side-way fall loading compared to isotropic QCT-based FE models of human femurs, J. Mech. Behav. Mater. 32 (2014) 287–299.
[47] J.H. Keyak, S.A. Rossi, K.A. Jones, H.B. Skinner, Prediction of femoral fracture load using automated finite element modelling, J. Biomech. 31 (2) (1997) 125–133.
[48] D. Dragomir-Daescu, J. Op Den Buijs, S. McEligot, Y. Dai, R.C. Entwistle, C. Salas, L.J. Melton, K.E. Bennet, S. Khosla, S. Amin, Robust qct/fea models of proximal femur stiffness and fracture load during a sideways fall on the hip, Ann. Biomed. Eng. 39 (2) (2011) 742–755.
[49] J.E.M. Koivumäki, J. Thevenot, P. Pulkkinen, V. Kuhn, T.M. Link, F. Eckstein, T. Jämsä, CT-based finite element models can be used to estimate experimentally measured failure loads in the proximal femur, Bone 50 (4) (2012) 824–829.
[50] A.D.P. Bankoff, Biomechanical characteristics of the bone, human musculoskeletal biomechanics Tarun Goswani, IntechOpen (2012), https://doi.org/10.5772/19690 Available from: https://www.intechopen.com/books/human-musculoskeletal-biomechanics/biomechanical-characteristics-of-the-bone.
[51] N. Vilayphiou, S. Boutroy, P. Szulc, B. Van Rietbergen, F. Munoz, P.D. Delmas, R. Chapurlat, Finite element analysis performed on radius and tibia HR-pQCT images and fragility fractures at all sites in men, J. Bone Miner. Res. 26 (5) (2011) 965–973.
[52] M.G. Ascenzi, J. Chin, J. Lappe, R. Recker, Non-osteoporotic women with low-trauma fracture present altered birefringence in cortical bone, Bone 84 (2016) 104–112.
[53] K.C. Chung, S.V. Spilson, The frequency and epidemiology of hand and forearm fractures in the United States, J. Hand Surg. Am. 26 (5) (2011) 908–915.
[54] D. Jerrhag, M. Englund, K.K. Magnus, B.E. Rosengren, Epidemiology and time trends of distal forearm fractures in adults – a study of 11.2 million person-years in Sweden, BMC Musculoskelet. Disord. 18 (1) (2017) 240.